Ke, X. and V.A. Baki, (2021) Microporous Mesoporous Mater., 325:111329.
https://doi.org/10.1016/j.micromeso.2021.111329

Assessing the suitability of alkali-activated metakaolin geopolymer for thermochemical heat storage

Xinyuan Ke*, Vahiddin Alperen Baki

Department of Architecture and Civil Engineering, University of Bath, Bath BA2 7AY, United Kingdom

Corresponding email: x.ke@bath.ac.uk

Abstract

This study investigates the suitability and potentials of using alkali-activated metakaolin geopolymers as sustainable low-cost thermochemical heat storage materials via water sorption and/or hydration reactions. Four different alkali-activated metakaolin geopolymer formulations were assessed. The cyclic water sorption capacity and moisture diffusion coefficients were assessed via two continuous water vapour sorption/desorption cycles using the dynamic water vapor sorption (DVS), proving the regeneration ability of geopolymers for sorption thermal energy storage. The thermochemical properties of geopolymers, including the dehydration enthalpy and activation energy, were determined. For the amorphous sodium aluminosilicate hydrate gel (N-A-S-H) with bulk Si/Al ratio of 1.5, the mass and volumetric energy storage capacity of 827.9 $J/g_{hydrate\ sample}$ and 350 $kW{\cdot}h/m^3$ were achieved, with a charging temperature of around 120 °C. The outcomes of this study suggest that alkali-activated metakaolin geopolymers have the potential to be used for both low-temperature water sorption thermal energy storage and medium temperature hydration/dehydration thermochemical energy storage. The energy storage performances of metakaolin geopolymers are closely related to their aluminosilicate framework structures and surface textural properties. The partial crystallisation of the amorphous N(K)-A-S-H gel, resulting in the formation of micropores, which does not seem to affect the maximal water uptake but increases the proportion of the chemically bound water. The presence of the amorphous mesoporous aluminosilicate gel N(K)-A-S-H gel in geopolymers leads to desorption hysteresis at relative humidity higher than 30%. Further optimisation of the synthesis approach, aluminosilicate framework structures, micro and mesopore structures will be required to optimise their overall thermal energy storage performances.

Keywords: Mesoporous aluminosilicate hydrates, dynamic water sorption, alkali-activated geopolymer, thermochemical heat storage.

1. Introduction

The use of renewable clean energy such as solar energy will significantly improve the sustainability and reduce the CO_2 emissions from the construction and building sectors [1, 2]. The effective recovery, stable storage, and efficient reuse of heat derived from solar energy incident on building surfaces play indispensable roles in achieving net-zero buildings [3]. The current thermal energy storage materials include sensible heat storage materials (e.g. concrete, clay) [4], latent heat storage materials (e.g. PCM) [5] and thermochemical heat storage

materials (e.g. zeolites, metallic salts) [6, 7], where the thermochemical heat storage materials generally possess the highest volumetric energy density. The controllable charging/discharging processes in thermochemical heat storage materials makes it particularly preferrable as long-term/seasonal thermal energy storage materials for integrated solar energy system [8, 9].

The thermochemical energy storage relies on chemical reactions, mainly water vapor or gas sorption reactions, to storage heat as chemical potential energy [10]. Zeolites [11], salt hydroxides [12], salt hydrates [13], and ettringite minerals [14] have been widely investigated as thermochemical energy storage materials. The recent studies have demonstrated that the use of salt implemented composite materials have better chemical and thermal stability due to the support provided by the porous host materials [15], such as the $MgSO_4$ impregnated zeolite X [16, 17], K_2CO_3 impregnated vermiculite [6], silica gel containing $CaCl_2$ [7], $MgSO_4$ impregnated zirconia ceramic composites [18], as well as the $CaCl_2$ impregnated metal–organic framework [19]. Despite of significant advantages of thermochemical energy storage technique in domestic applications, the challenges remain in the design of low-cost, highly-efficient and easy to operate thermochemical energy storage materials [20, 21]. For achieving net-zero buildings, resource efficiency and minimised embodied carbon in buildings will also need to be considered in addition to the energy efficiency. While decreasing the operation carbon emission, the improve of building energy efficiency with new technologies and advanced materials can increase the overall embodied carbon (of the life cycle emission) of buildings from 20% to as high as 50%-90% percent [22]. Porous host materials, such as zeolites, zirconium ceramics and metal-organic framework materials, despite of their satisfactory performances, are expensive and with high embodied carbon [23]. The importance of sourcing new low-cost sustainable materials for thermal energy storage has been highlighted in recent the study [20] as one of the main challenges faced by the implementation of thermochemical heat storage materials for domestic energy storage.

Alkali-activation is a versatile chemical synthesis route that can effectively utilise a wide range of aluminosilicate-rich mineral resources, such as calcined clays [24], industrial ashes [25], natural minerals [26], and mine tailings [27]. Strong alkaline solutions, such as sodium/potassium hydroxides, sodium/potassium silicates, are often used as activators [28], while near-neutral and acidic activators can also be used depending on the chemistry of the precursors [29, 30]. When aluminosilicate precursors with low Ca and Mg content (<10 wt%) are used, amorphous alkali aluminosilicate hydrates form as the main reaction products, which are also been called geopolymers [28]. These amorphous alkali aluminosilicate hydrates consist of tetrahedrally-coordinated framework aluminosilicate gels with pseudo-zeolitic nanoscale structures [31-33], which are often referred to as N-A-S-H or K-A-S-H gels using the cement chemist notation when sodium or potassium type activator is been used.

Geopolymers produced from low-Ca content precursors possess superior thermal resistance up to 1000 °C [33, 34]. Upon heating, the water in the aluminosilicate hydrate gels, including both the interstitial water (or physically adsorbed) and the chemically bound water, decompose and escape the aluminosilicate gel structure at temperature below 400 °C -600 °C [33, 34]. When been heated to above 1000 °C, geopolymers transform to different ceramic phases as the results of different types of extra-framework cations. Such as nepheline [34], leucite [33], and pollucite [31] from sodium, potassium and caesium based geopolymers. The atomic-level investigation of the alkali-activated metakaolin revealed that non-structural changes were observed from the aluminosilicate framework at temperatures below 400 °C [31, 33], similar

to the dehydration process commonly identified in zeolites upon heating [35]. This suggests that the main components in geopolymers, N-A-S-H and/or K-A-S-H gels, might be able to perform as thermochemical energy storage materials via water sorption and/or hydration processes, where heat can be stored when been heated at below 400 °C and released in the form of hydration heat for utilisation when in contact with water again. However, despite dehydration does not change the aluminosilicate framework structure of geopolymer gels, it is currently unknow if the dehydrated geopolymer gel can be rehydrated, and whether this dehydration/rehydration processes are reversible. In addition, the effects of partial pressure of water vapor (relative humidity) on the kinetic of dehydration/rehydration processes of geopolymers have not been investigated. All these are important factors that will determine the heat storage capacities and efficiencies of geopolymers as thermochemical heat storage materials.

This study assessed the suitability of four metakaolin geopolymers with different chemical compositions and gel structure properties as thermochemical energy storage materials by investigating these standing questions via experimental methods. The cyclic water sorption/desorption kinetics were investigated through the dynamic water vapor sorption test. The dehydration enthalpy and activation energy of these four metakaolin geopolymers were determined from the thermogravimetry analysis and the differential scanning calorimetry. Based on the experimental results, the theoretical mass and volumetric energy densities of the four geopolymer gels were estimated. The correlations between the chemistry, the surface textural properties of these geopolymer gels and their thermochemical heat storage performances were also discussed.

2. Materials and methods

2.1. Sample preparation

The alkali-activated metakaolin was prepared by mixing aqueous alkali solutions with metakaolin (MetaStar 501, Imerys UK) to obtain a stoichiometry of $M_2O{\cdot}Al_2O_3{\cdot}nSiO_2{\cdot}11H_2O$, where M refers to alkali metal cations (Na or K). Three different alkali-activators solutions were used in this study, two non-siliceous activators (NH and KNH) and one siliceous activators (NS), prepared from NaOH (Honeywell Fluka, ≥98%) pellets, KOH (Sigma-Aldrich, >90%) pellets, and sodium silicate solution (SiO_2/ Na_2O ratio of 2.0, water content of 56%) supplied by PQ Corporation. The required amount of Milli-Q water was added to the alkali-activator solution to obtain a constant M_2O/H_2O ratio in each sample. The mixtures were blended using a high shear overhead mixer, cast and sealed in centrifuge tubes, and stored under designated conditions prior to analysis. Table 1 summarised the stoichiometry designs and aging conditions of the four alkali-activated metakaolin prepared in this study. Sample NH20 and KNH20 were activated by sodium hydroxide and mixed (1:1) sodium hydroxide and potassium hydroxide respectively, and stored at 20±2 °C. Both sample NS20 and NS80 were activated by sodium silicate solution (NaOH pellets + commercial sodium silicate solution). While NS20 was stored at 20±2 °C, NS80 was stored at 80±2 °C for 80 °C for 1 year followed by storage at 20±2 °C. These four samples were selected for assessing the impact of activator cations, Si/Al ratio and the aluminosilicate gel structures on the thermochemical energy storage performances of alkali-activated metakaolin geopolymers. All samples were assessed at the curing age of three years for representing the long-term performances.

Table 1 Stoichiometry designs and aging conditions of the four alkali-activated metakaolin prepared in this study. The values shown in this table are atomic ratios.

	Si/Al	M_2O	SiO_2/M_2O	H_2O/M_2O	Temperature	Age
KNH20	1.01	K_2O:Na_2O=1:1	0.28	11	20 °C	3yr
NH20	1.01	Na_2O	0.28	11	20 °C	3yr
NS20	1.51	Na_2O	1.28	11	20 °C	3yr
NS80	1.51	Na_2O	1.28	11	80 °C for 1 year followed by 20 °C	3yr

2.2. Testing methods

The gel structures of the alkali-activated metakaolin geopolymers prepared in this study were assessed using powder X-ray diffraction (XRD) and Fourier-transform infrared spectroscopy (FTIR). The XRD was performed on a STOE STADI P (Cu radiation, λ=1.54 Å) instrument in transmission mode. The X-ray generator was operating at 40 kV and 40 mA. The diffraction results were recorded from 5° to 75° (2θ), with a step resolution of 0.015° (2θ) per step. A double Mythen detector was used, where each detector covers a range of 19° (2θ) and operated at 31.6 seconds per degree (2θ). Each XRD scan took around 20 minutes. The FTIR spectra were performed using the Perkin Elmer Frontier instrument with the transmission cell. The samples were prepared using the KBr method (powdered geopolymer ground with KBr solids to make pressed pellets). The transmission spectra were recorded from wavenumber 400 cm^{-1} to 4000 cm^{-1}, with 16 repeated scans for each spectrum acquisition.

The surface textural properties of geopolymers were characterised via N_2 gas sorption at 77K using the Autosorb-iQ-C by Quantachrome Anton Paar. Prior to the gas sorption test, the powdered samples were degassed at 300 °C for 12 hours to fully dehydrate the samples. The pore size distribution (PSD) was determined using the heterogeneous surface non-local density function theory (NL-DFT) model using the Demo version of the SAIEUS software (www.nldft.com/download/) (Micromeritics, GA). The slit type pore structure was chosen based on the shape of N_2 sorption results [36]. The SAIEUS optimise the adjustable fitting parameter λ according to the L-curve method [37], which balances the roughness of the solution and the goodness of the fit. The Brunauer–Emmett–Teller (BET) surface areas were calculated from the N_2 gas sorption data.

The water sorption kinetics of geopolymers were assessed via dynamic (water) vapor sorption (DVS) within the relative humidity range of 0% to 95% at 25 °C. The DVS Advantage instrument (Surface Measurement Systems) was used. In order to assess the cyclic water sorption performances and regeneration ability of geopolymers, two stepwise dynamic water sorption-desorption circles were performed. Prior to the first circle, the samples were pre-dried at 200 °C (maximal temperature achievable by the instrument) until constant weight to fully dehydrate the geopolymers. No drying stage was applied between the first and the second circle. The moisture diffusion coefficients as a function of relative humidity were calculated based on the DVS results using the Slope Method suggested by [38].

The dehydration enthalpy and activation energy of geopolymers were assessed combining thermogravimetric analysis (TGA) using the STARe system analyser from the Mettler Toledo, and the differential scanning calorimetry (DSC) using the DSC Q20 instrument from TA

Instruments. For TGA analysis, the samples were first kept under 30 °C for 1 hour, then ramped from 30 °C to 400 °C at constant heating rate and then held at 400 °C for another 1 hour. Each sample was measured under heating rate of 2K/min, 4 K/min and 10 K/min respectively under N_2 gas atmosphere (gas flow rate 60 ml/min) for determining the activation energy. For the DSC analysis, two heating ramps were performed. The samples were first kept under 25 °C for 30 minutes to reach equilibrium, then ramped from 25 °C to 395 °C (maximal temperature achievable by the instrument) at a content heating rate of 10K/min, held at 395 °C for 15 minutes (the first ramp) and cooled done to 25 °C, then held at 25 °C for another 15 minutes and ramped to 395 °C again at the same heating rate (the second ramp).

3. Results and discussion

3.1. Structural properties of geopolymers

The mineralogy and gel structures of the four geopolymer gels investigated in this study were assessed using the XRD (Figure 1) and the FTIR (Figure 2) respectively, for characterising their crystalline structure and the chemical bonds. The XRD results show that metakaolin activated with non-silicious activators under room temperature for 3 years, NH20 and KNH20, resulted in formation of significant crystallised zeolitic phases. The main zeolitic phase identified in NH20 was FAU-type zeolite (zeolite-X(Na), Powder Diffraction File, PDF# 00-039-0218) with a smaller amount of LTA-type zeolite (LTA-Na, PDF# 01-073-2340). For KNH20, similar amount of FAU-type zeolite (zeolite-X(Na), and/or zeolite-X(K), PDF# 00-026-0898) and CHA-type zeolite (chabazite K, PDF# 01-085-0976) were formed. A small fraction of amorphous hump centred at around 31° (2θ) was identified in KNH20, suggesting the presence of a small amount of amorphous sodium/potassium aluminosilicate hydrate (N(K)-A-S-H). The FAU-type zeolite framework can accommodate both/either Na^+ and/or K^+ as extra-framework cations [39], with higher tendency to form chabazite K through inter zeolite conversion [40]. Since in sample KNH20 the molar ratio of Na to K element is 1, the reflection peaks have been assigned to both K charge-balanced and Na charge-balanced FAU-type zeolite. The formation of LTA-type and FAU-type zeolite are commonly identified in sodium hydroxide activated geopolymers [41, 42], the formation of which can be accelerated to 24 hours under hydrothermal curing conditions [41]. The formation of chabazite K is commonly identified in geopolymers (partially) using potassium type alkali activators [42, 43]. For the metakaolin geopolymers activated with silicious activators and stored under room temperature, NS20 showed only a broad hump centred at around 29° (2θ) corresponding to the amorphous sodium aluminosilicate hydrate (N-A-S-H). The small fraction of anatase (TiO_2, PDF# 01-084-1286) and quartz (SiO_2, PDF# 01-078-2315) are impurities from the metakaolin raw materials. Sample NS80 was designed to represent the partially crystallised geopolymer prepared using silicious activators. Since the partial crystallisation of sodium silicate activated geopolymers normally takes very long time (>5 years), the NS80 was hydrothermally aged for 1 year and move to ambient storage for the purpose of accelerating the partial crystallisation. As shown in Figure 1, the poorly crystallised phases in NS80 have similar crystalline structure to the NH20 samples, but NS80 still contains a significant amount of amorphous aluminosilicate gels.

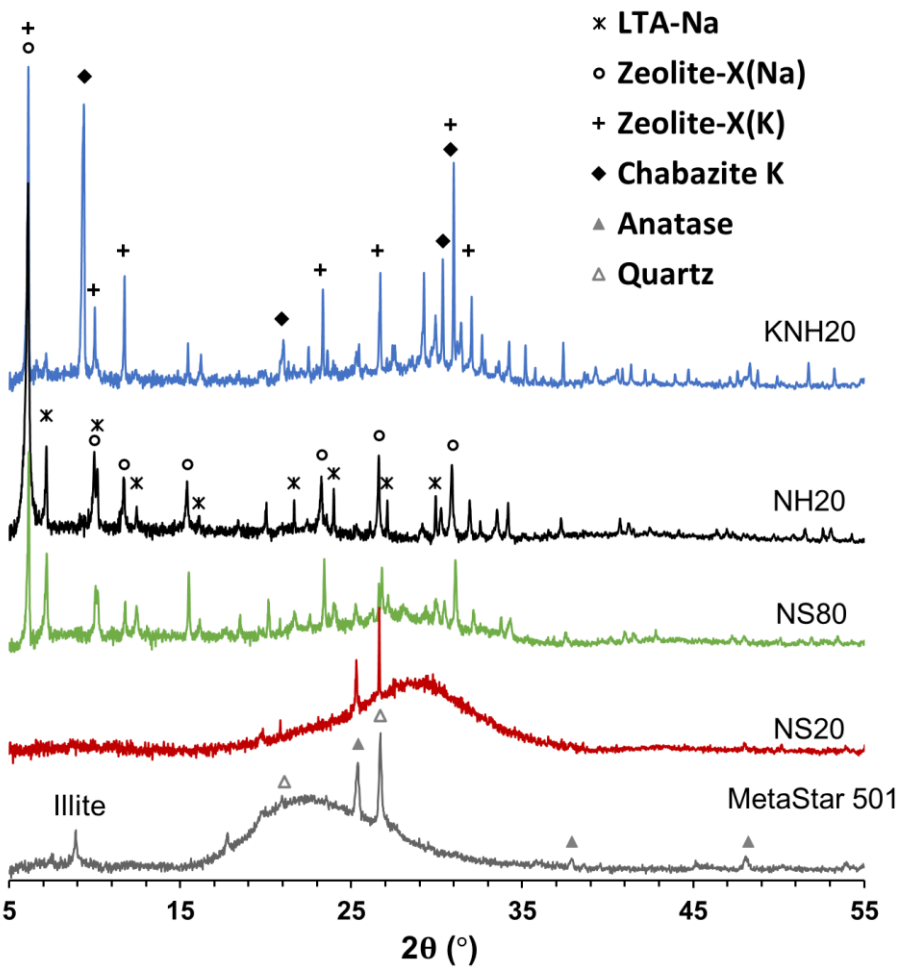

Figure 1 X-ray diffraction patterns of the four alkali-activated metakaolin geopolymers.

The FTIR results (Figure 2) correspond with the XRD results. The FTIR bands between the 900 to 1200 cm^{-1} region correspond to the asymmetric stretching vibration of Si-O-T (Si/Al), where the increase of Al substitution in the tetrahedral silica site leads to shifting of the spectra to lower wavenumbers [35, 44]. For samples NH20 and KNH20 with the bulk Si/Al ratio of 1.0, the main Si-O-T band within this region is centred at 985 cm^{-1}; while for NS20 and NS80 with bulk Si/Al ratio of 1.5 the main Si-O-T band within this region is centred at 995 cm^{-1}. The shoulder at 1146 cm^{-1} in sodium silicate activated samples is likely attributed by the asymmetric stretching vibrations of Si-O-Si bonds [44, 45], as a result of the higher silica content. The FTIR bands between the 450 to 750 cm^{-1} region are characteristic to the ring structures of the aluminosilicate frameworks [44]. For both NH20 and KNH20, the bands at 751 cm^{-1}, 661 cm^{-1}, and 554 cm^{-1} are characteristic for the FAU-type zeolite, corresponding to the double-4-members-ring (D4R) structures [44]. For the NS20 and NS80, less well-defined FTIR bands were identified within this spectra range, where 696 cm^{-1}, 585 cm^{-1}, and 445 cm^{-1} correspond to the presence of 4-members-ring structures in the disordered states within these solid powders [45]. The band at around 1646 cm^{-1} corresponds to the bending vibration of water molecules [44]. Different band shapes and relative intensities (to the main Si-O-T band) of the water molecules band in each sample suggest different chemical environment and

quantity of water in these samples, which will be discussed and quantified in the following sections.

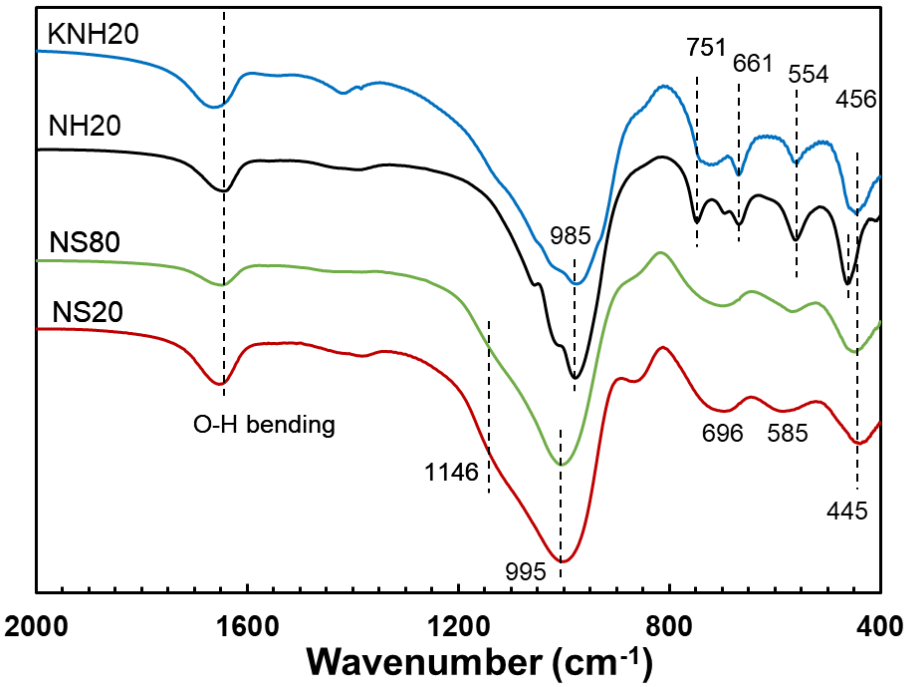

Figure 2 FTIR spectra of the four alkali-activated metakaolin geopolymers.

3.2. Surface textural properties

The surface textural properties of the four geopolymers investigated in this study are summarised in Table 2, including the BET surface areas, the diameter of the micropores, the diameter/range of the mesopores, and the total pore volumes calculated based on the NL-DFT pore size distribution model. The results shown that sample NH20 has the highest BET surface area, followed by KNH20, NS80 and NS20. The N_2 sorption/desorption isotherms are shown in Figure 3A, together with the pore size distribution calculated based on the sorption data (Figure 3B). The N_2 sorption isotherms indicate significant N_2 gas sorption at relative pressure near zero in sample NH20, which is less significant for sample KNH20 and NS80; while sample NS20 showed negligible N_2 sorption volume change within this region. The N_2 gas sorption at relative pressure near zero correspond to the sorption of N_2 gas molecules in the micropores, where higher sorption volumes indicate higher pore volumes. As shown in Figure 3B, sample NH20 contains the highest amount of micropore with pore diameter of 5.7 Å, while sample KNH20 and NS80 contain smaller amount of micropores but with similar pore diameters, 5.6 Å and 5.0 Å respectively. The results for NS20 suggest the absence of the micropores in this amorphous gel, consistent with the non-crystalised geopolymer gels reported in literature composed of different bulk chemical positions [46]. The presence of micropores in crystallised and partially crystallised geopolymer samples is likely contributed by the zeolitic structure, consistent with the results reported for sodium hydroxide activated metakaolin geopolymer in literature [47]. The N_2 sorption volume increases at higher relative pressure

indicate the presence of mesopores in all four samples, which are mostly within the diameter range between 24 to 60 Å (Table 2). The mesopore volume is higher for NH20, but similar for the other three samples. The overall shapes of the N_2 gas sorption isotherms suggest that the mesopores in the geopolymer gels are in slit-type shapes [36]. In addition, only sample NS20 showed significant desorption hysteresis while the other three samples only showed slight desorption hysteresis. The desorption hysteresis is commonly observed from the amorphous aluminosilicate gel prepared from alkali-activated metakaolin [46], which is likely caused by the presence of ink-bottle type of pores. The total pore volume calculated based on the NL-DFT pore size distribution model suggest that sample NH20 has the highest total pore volume, which is about four time higher than the other three samples. Despite the differences in pore size distribution and surface areas, the calculated pore volume of the other three geopolymer samples are relatively similar (Table 2).

Table 2 Summary of the surface textural properties of the four alkali-activated metakaolin geopolymer assessed.

Sample ID	S_{BET} (m^2/g)	Micropore diameter (Å)	Mesopore diameter/range (Å)	Total pore volume (Sorption, NL-DFT) (cm^3/g)
KNH20	119.2	5.7	25.8-51.1	0.131
NH20	531.4	5.6	28.8-59.7	0.406
NS80	66.9	5.0	24.1-35.9	0.115
NS20	42.1	None	28.8	0.102

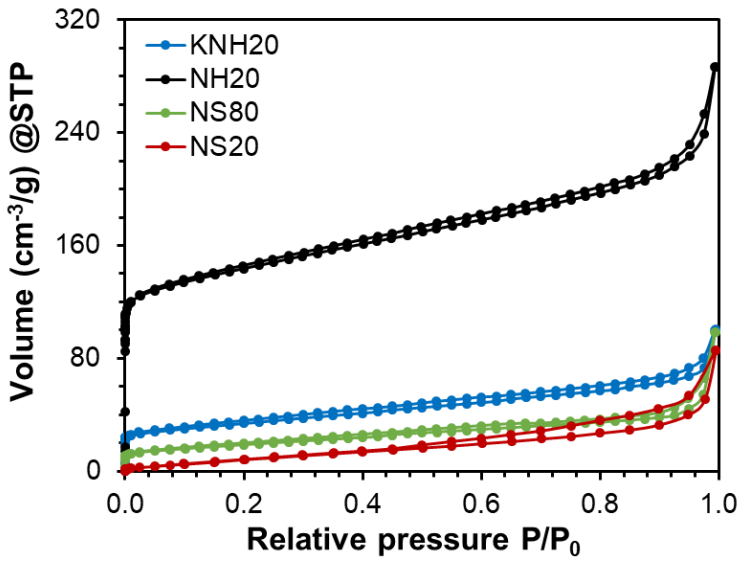

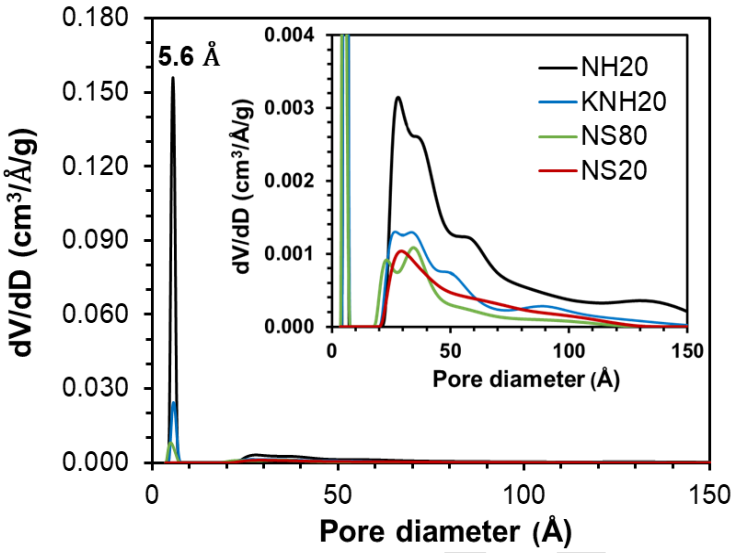

Figure 3 (A) N2 gas sorption/desorption isotherms and (B) pore size distribution calculated using the heterogenous surface NL-DFT model.

3.3. Cyclic water sorption/desorption kinetics

The water sorption/desorption kinetics of the four metakaolin geopolymer gels under two consecutive sorption/desorption circles were assessed using an automated dynamic water vapor sorption instrument. The water vapor sorption isotherms of each sample are shown in Figure 4, where the dry mass (after pre-dried at 200 °C) of each sample is used as the reference mass (shown as 0%).

As shown in the results (Figure 4), all of these four geopolymer samples assessed in this study: 1) have the ability to rehydrate after dehydration at 200 °C; 2) the maximal water uptakes at 95% relative humidity are within marginal differences (<0.2 wt.%) for the same sample pre-treated at either 200 °C (first circle) or 25 °C (second circle) at 0% relative humidity; 3) the desorption isothermal for both circles are almost identical with negligible (<0.2 wt.%) increase in final water content at 0% relative humidity. These performances suggest that alkali-activated metakaolin geopolymers have the ability to perform cyclic hydration/dehydration and reach the same maximal water uptake capacities at 95% relative humidity, with and without dehydration pre-treatment. The results prove that, despite the different chemical compositions, gel structures, and surface textural properties, the alkali-activated metakaolin geopolymers have the capacity to be used for both low temperature water sorption heat storage, as well as medium temperature (<300 °C) dehydration/hydration thermochemical heat storage.

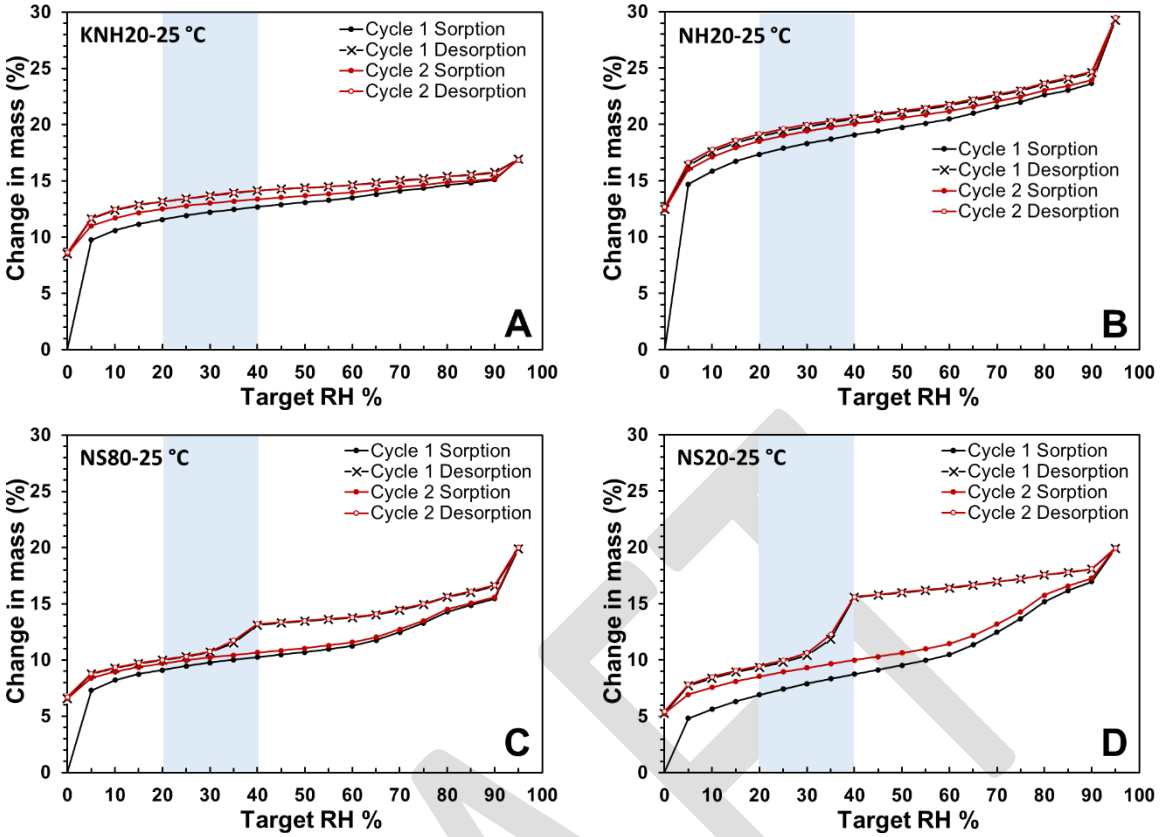

Figure 4 Water vapor sorption isotherms during two sorption/desorption circles. (A) KNH20, (B) NH20, (C) NS80, (D) NS20.

However, the overall water uptake capacity, desorption behaviours and moisture uptake kinetics are affected by the different chemical compositions, gel structures, and surface textural properties of these four samples assessed. Table 3 summarised the water uptake capacities of the four samples assessed during the two consecutive water sorption circles. It shows that sample NH20 has the highest maximal water uptake mass percentage (average 29.3 wt.%) comparing to its dry mass, while sample KNH20 has the lowest maximal water uptake percentage (average 16.9 wt.%). Sample NS80 and NS20 have about the same maximal water uptake percentage (average 19.9 wt.%). Correlating with the gel structure and the surface textural properties, it appears that in general Na-based geopolymers have higher water uptake capacity while the replacement of Na-based activator with K-based activator decreases the water uptake capacity. The total pore volume of each sample is positively correlated with the water uptake capacity, however less critical than the activator chemistry as the KNH20 has the second highest total pore volume but the lowest water uptake capacity. The presence of micropores, which links to the partial crystallisation of the N-A-S-H gel, does not seem to affect the maximal water uptake capacity but critical to the amount of chemically bound water that is independent of relative humidity changes. Regardless of the activator chemistry, the presence of amorphous N(K)-A-S-H gel can decrease the amount of chemically bound water remained at 0% relative humidity, with the fully amorphous sample NS20 showing the lowest value (Table 3). The mass change differences between the first and the second sorption curve at below 90% relative humidity, as observed from all samples, suggest that the chemically bound water sites vacated by pre-drying at 200 °C will be reoccupied at different relative

humidity. But the rehydration of more than 80% of the sites can be achieved at relative humidity as low as 5% in sample NH20, KNH20 and NS80, while rehydration of more than 60% of the sites can be achieved in sample NS20 at the same relative humidity.

In addition, NS80 and NS20 showed significant desorption hysteresis at relative humidity higher than 30%, which is most likely due to the presence of amorphous N-A-S-H gels with higher Si/Al ratio (around 1.5). This corresponds with the nitrogen adsorption/desorption isotherms, where desorption hysteresis was also observed in these two samples. In comparison with nitrogen desorption hysteresis, more significant water vapour desorption hysteresis was observed from these samples, which is likely due to the differences in contact angles and adsorption energy [48, 49]. Similar desorption hysteresis behaviours have also been observed from shale rocks where quartz were the main mineral composition [50]. The desorption hysteresis might be caused by the tensile strength effect of the adsorbed phase, the interconnection and tortuosity of the pore structures and possible existence of "ink bottle" pores [51]. For the sample NS80 and NS20, the dominate effects might be the presence of "ink bottle" pores, which were observed in literature via combined nitrogen sorption and small-angle neutron scattering [46]; however the effects from the other two mechanisms cannot be excluded based on the results from this study. The desorption hysteresis is more significant at relative humidity between 30%-60% than at higher relative humidity, which might relate to the fact that there is stronger van der Waals interactions between the condensed fluid and the pore walls in smaller pores [50].

Table 3 Summary of the water sorption/desorption capacities (in percentages) of the four metakaolin geopolymer assessed. The dry mass (pre-dried at 200 °C) of each sample is used as the reference mass (shown as 0%).

	KNH20 wt.% (dry mass)	NH20 wt.% (dry mass)	NS80 wt.% (dry mass)	NS20 wt.% (dry mass)
Maximal mass increase during 1st sorption cycle	16.95	29.24	19.87	19.89
Maximal mass increase during 2nd sorption cycle	16.88	29.46	20.03	19.95
Final mass change after 1st desorption	8.52	12.45	6.59	5.27
Final mass change after 2nd desorption	8.63	12.69	6.70	5.44
Average mass change due to RH changes	8.34	16.78	13.30	14.57
Average water uptake independent of RH changes	8.58	12.57	6.64	5.36

The moisture diffusion coefficients on the surface of these four geopolymer gels (Figure 5) calculated from the dynamic water sorption mass change curves were based on the simplification that water diffused into a thin slab of geopolymer powder samples from one side. During the DVS experiments, the tested samples formed a thin slab in the sample pan with moisture diffusion occurring via the top surface. Therefore, the one-dimensional slab model should be applied instead of the spherical diffusion model (where sample particles will be expected to be individually distributed on the sample pan). In this study the moisture diffusion coefficients were calculated by numerically solving the Fick's second law for one-dimensional water diffusion into a thin slab of powder samples, also known as the Slope Method [38]. Eq. 1 and Eq. 2 can be used to calculate the diffusion coefficient during water sorption and desorption, where t is the time increment from last equilibrium; M_0, M_e and M_t are the mass

values at end of previous equilibrium stage (initial mass of the new stage), at equilibrium at the current stage, and mass at time *t*; *l* is the thickness of the powder sample on the sample pan and *D* is the diffusion coefficient under the condition of current stage. Detailed deduction of the numerical methods can be found in [38].

$$\frac{M_t}{M_e} = 2\left(\frac{Dt}{\pi l^2}\right)^{1/2} \quad \text{(For sorption process, when } \frac{M_t}{M_e} < 0.6\text{)} \qquad \text{Eq. 1}$$

$$\frac{M_t - M_e}{M_0 - M_e} = 1 - 2\left(\frac{Dt}{\pi l^2}\right)^{1/2} \quad \text{(For desorption process, when } 0.4 < \frac{M_t - M_e}{M_0 - M_e} < 1\text{)} \qquad \text{Eq. 2}$$

As shown in Figure 5, the moisture diffusion coefficients for the four samples assessed vary at different relative humidity under sorption or desorption conditions, but all within the range between 10^{-9} to 10^{-8} m^2/s. In general, the diffusion coefficients are higher within the medium relative humidity ranges (30%-60% RH), but lower at either low or high relative humidity. The moisture diffusion coefficients calculated from the second sorption process are always higher than that of the first sorption process, which might relate to the accessibility of water in the framework aluminosilicate gel surfaces. For samples with higher Si/Al ratio, NS80 and NS20, this phenomenon is more significant at relative humidity below 50%. The diffusion coefficients measured from the first and the second desorption mass changes are almost overlapped for all samples assessed. This can also support the hypothesis that the chemical sites occupied by the chemically bound water affect the water sorption/desorption kinetics, as for both desorption processes, the initial state of these samples (equilibrised at 95% relative humidity) were the same. In addition, it is very important to note that the desorption hysteresis at relative humidity above 30% leads to significant decrease of moisture diffusion coefficient between 20% to 40% relative humidity, the phenomena of which are more significant in samples with higher content of amorphous N(K)-A-S-H gels. This likely relates to the remove of condensed water in small pores within this relative humidity range [50]. However, beyond this relative humidity range, NS80 exhibited the highest overall diffusion coefficients followed by KNH20, NS20 and NH20. It appears that the presence of amorphous N(K)-A-S-H gels, which do not contain micropores in comparison to the well-crystalised zeolitic phases, promotes the water sorption kinetic to different extends instead of holding it back. In addition, the moisture diffusion coefficients calculated from these samples do not show a clear correlation with their surface properties. The significant higher diffusion coefficient identified from sample NS80 might due to the coupled effect of having both amorphous N-A-S-H gel and partially crystalised zeolitic structure. However, the type of charge balancing cations (e.g. K^+, Na^+) also appeared to play a significant role, as evidenced by comparing NS80 with KNH20 where both samples contain a mixed of amorphous and crystallised framework aluminosilicate phases. The higher water diffusion coefficient will lead to faster charging/discharging kinetics, and thus increasing the power of thermochemical energy storage materials. Therefore, the results shown in Figure 5 also suggest that relative humidity at around 40-60 % might be the most efficient condition for the water hydration/sorption thermochemical heat storage processes.

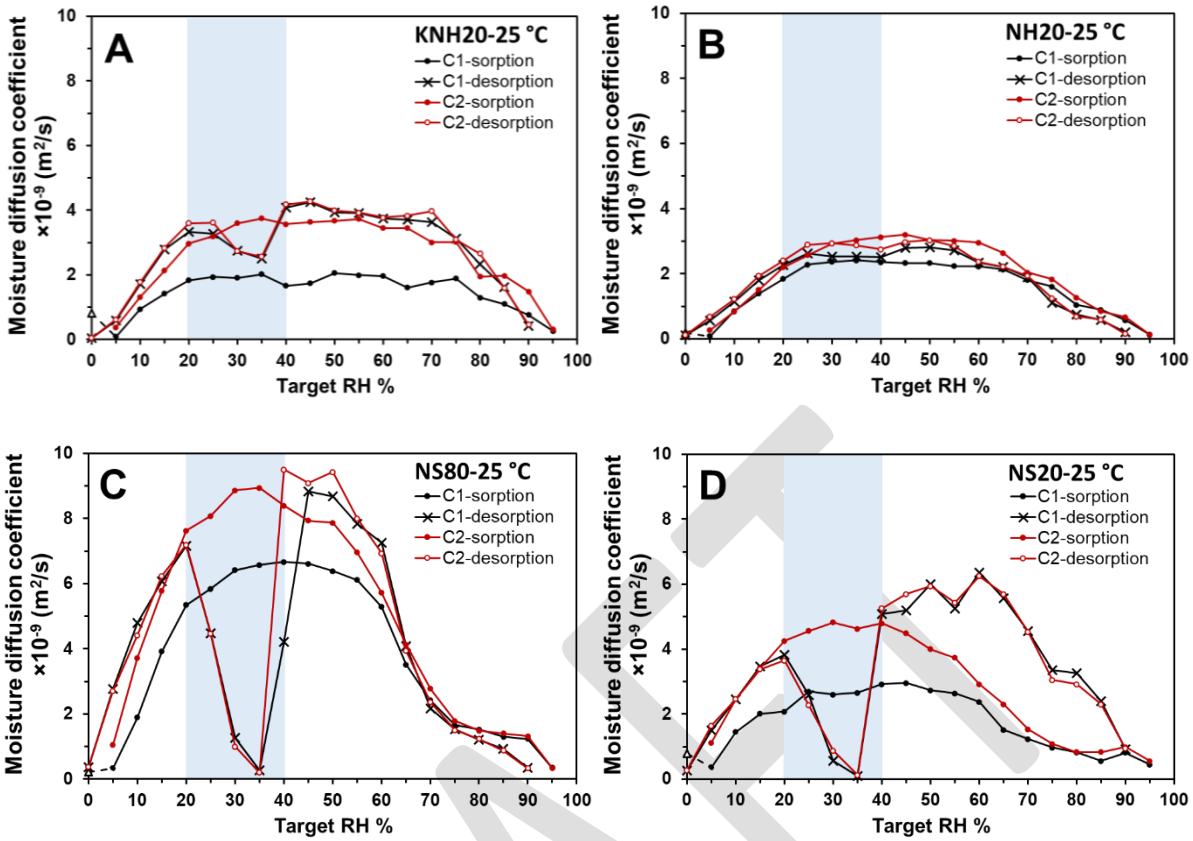

Figure 5 Moisture diffusion coefficients ($\times 10^{-9}$ m^2/s) during two sorption/desorption circles, estimated using the Slope Method [52] and plotted versus target relative humidity. (A) KNH20, (B) NH20, (C) NS20, (D) NS80.

3.4. Dehydration enthalpy and activation energy

The activation energy of dehydration for each sample were determined using both the Kissinger method [53] and the Ozawa method [54], as expressed by the Eq. 3and Eq. 4:

$$E_{activation} = R\frac{d\left(ln\left(\beta/T_p^2\right)\right)}{d\left(1/T_p\right)} \text{ (Kissinger method)} \quad \text{Eq. 3}$$

$$E_{activation} = -0.4567 \times R\frac{d\left(log(\beta)\right)}{d\left(1/T_p\right)} \text{ (Ozawa method)} \quad \text{Eq. 4}$$

, where β, T_p, and R are heating rate (K/min,) peak temperature (K) and gas constant (R=8.314 $J{\cdot}K^{-1}{\cdot}mol^{-1}$). Figure 6A and Figure 6B illustrate the TGA results of sample NS20 under three different heating rates, and the derived DTG results where the peak temperature (T_p) values were determined. The table of summary of the peak temperatures for the four samples assessed, including the calculation details of the Kissinger method and the Ozawa method, can be found in the Supporting Information. For sample KNH20 (Figure 6D), two distinctive DTG peaks during the dehydration process were observed and noted as $T_{p\text{-}1}$ and $T_{p\text{-}2}$. Then the activation energy can be calculated from the slops of the plots shown in Figure 7 using the Eq. 3and Eq. 4. The results are summarised in Table 4.

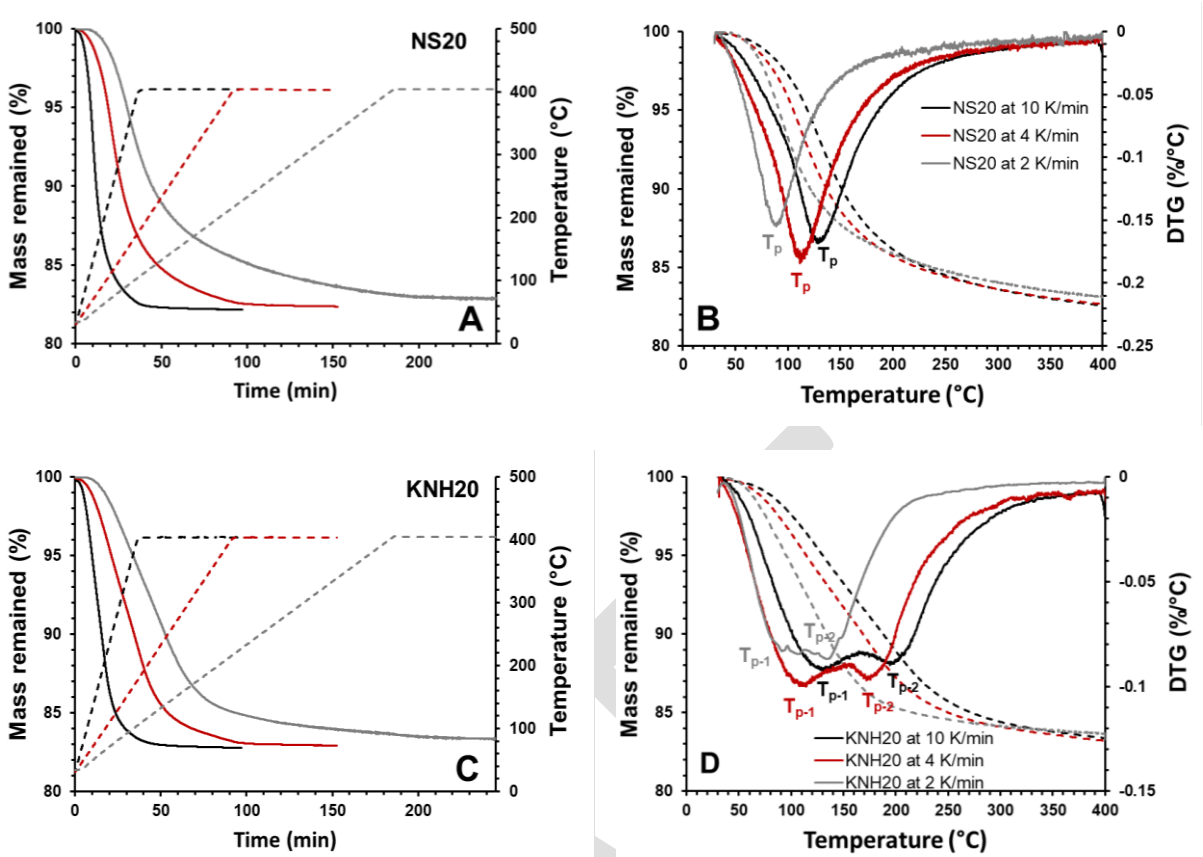

Figure 6 Thermogravimetric results of NS20 and KNH20 at three different heating rates, (A) and (C) heating program and mass change versus time; (B) and (D) determination of peak temperature (T_p) for each heating rate from the DTG curves.

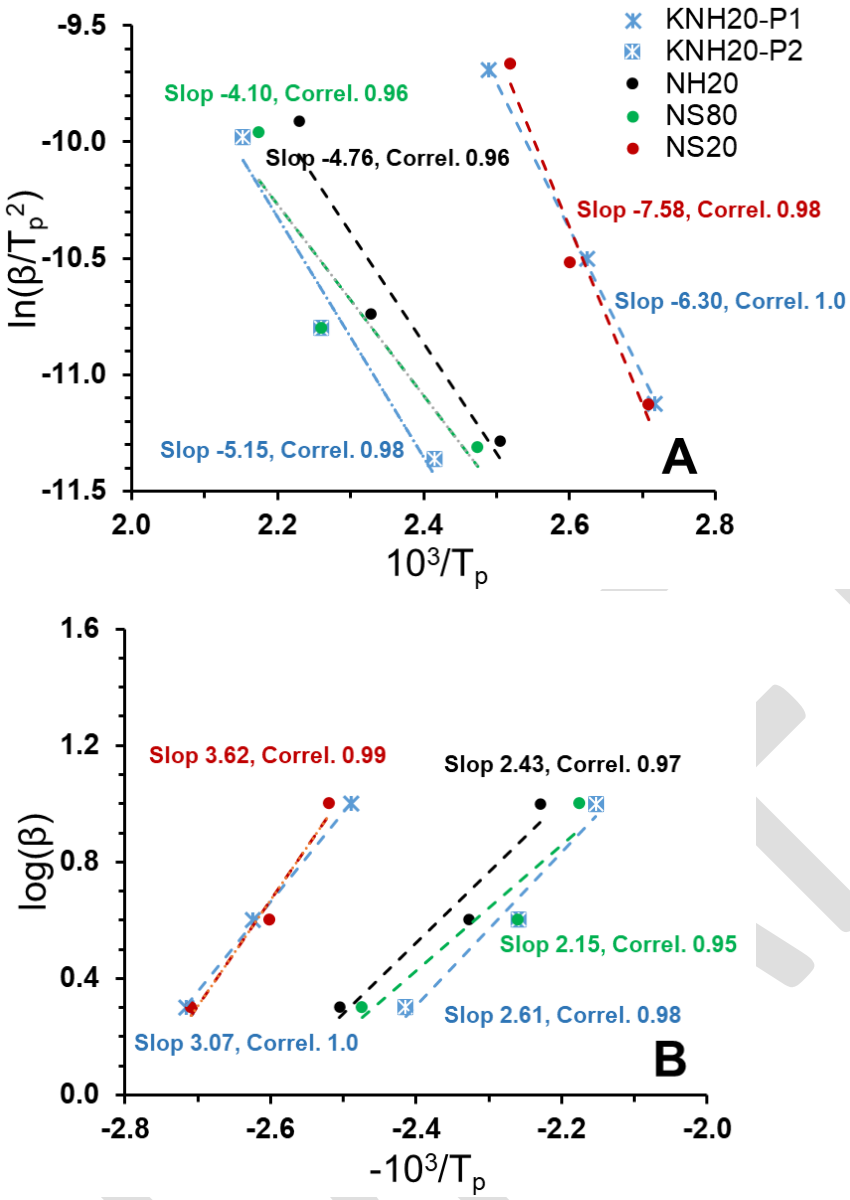

Figure 7 The (A) Kissinger and (B) Ozawa plots and linearised equations for the four geopolymer samples assessed in this study. The peak temperature values (T_p) were determined from the DTG results. There are two differential peaks identified from sample KNH20, the peak at below 150 °C is assigned to KNH20-P1 while the peak above 150 °C is assigned to KNH20-P2.

The dehydration enthalpy and the heat capacity of the dehydrated aluminosilicate geopolymers were determined using DSC with two consecutive heating ramps. The first heating ramp measures the total heat flow of dehydration which includes both the dehydration enthalpy and the sensible heat, while the second heating ramp measures only the sensible heat of the dehydrated geopolymers. Figure 8 illustrates the DSC results of the four geopolymer samples assessed as a function of the heating program. The dehydration enthalpy of each sample was determined by subtracting the total heat flow from the first ramp by the total heat from the second ramp. And the average heat capacity of the dehydrated aluminosilicate

geopolymer were determined from the sensible heat measured during the second ramp. The total mass loss due to dehydration within the temperature range between room temperature and 395 °C were determined from TGA, the value of which was used to determine the molar dehydration enthalpy. The thermodynamic properties determined from the DSC and TGA analysis are summarised in Table 4.

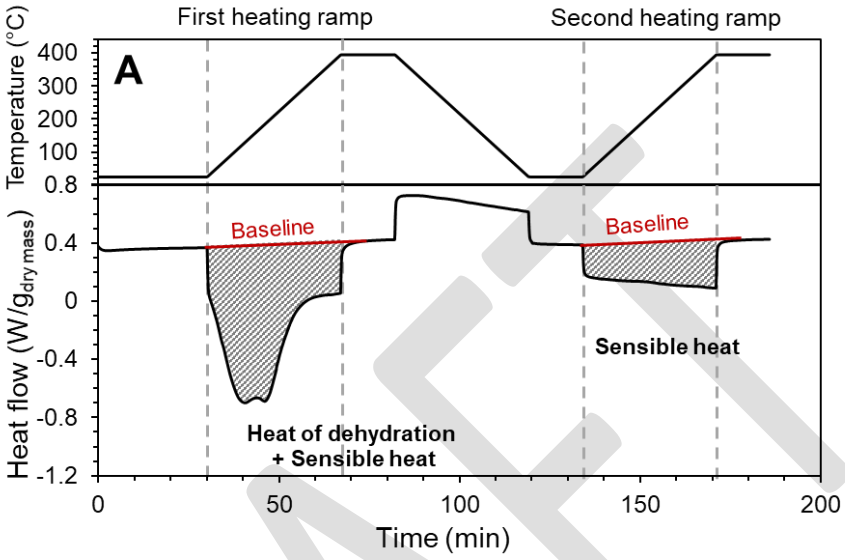

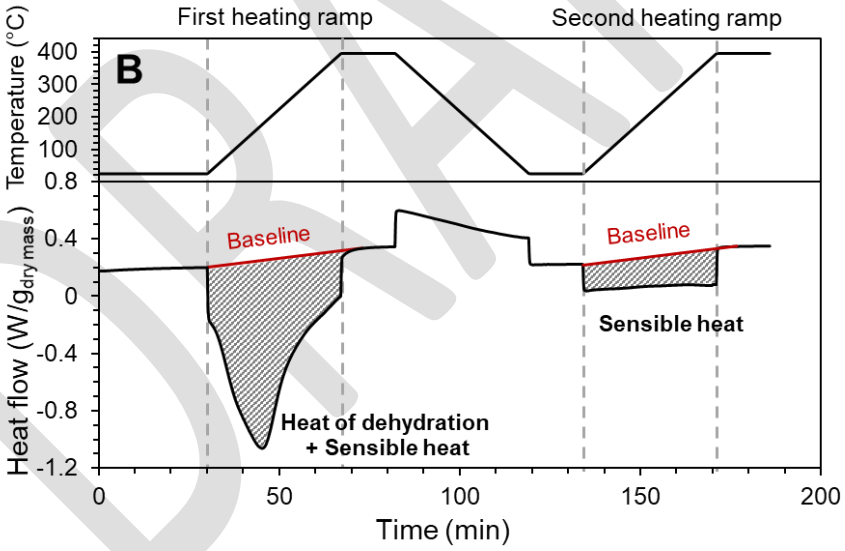

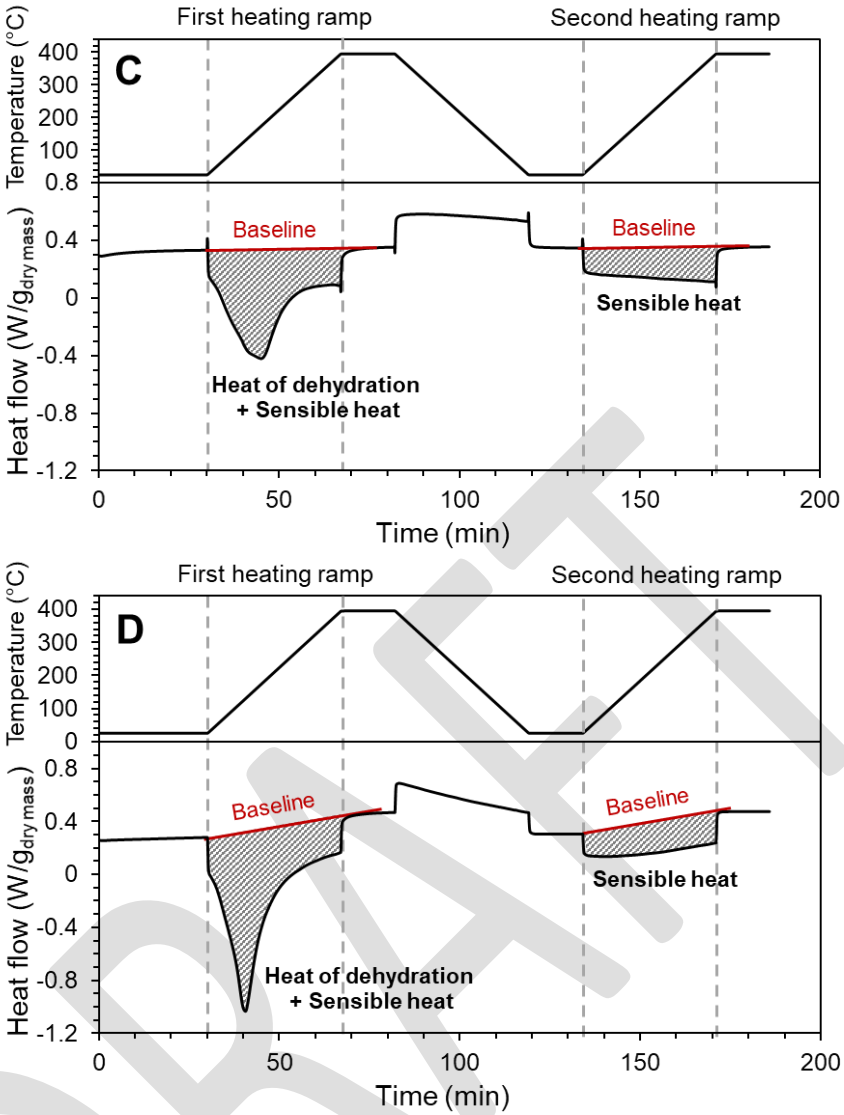

Figure 8 DSC results of sample (A)KNH20, (B)NH20, (C)NS80, (D)NS20 during two heating ramps as a function of time.

Table 4 The per molar and per mass (g) enthalpy of dehydration (< 400 °C), average heat capacity of dehydrate aluminosilicate, and activation energy of dehydration determined from two different methods.

Sample	$\Delta H_{dehydration}$ ($J/g_{dry\ mass}$)	$\Delta H_{dehydration}$ (kJ/mol_{H2O})	$Cp_{dehydrated}$ (J/kg·K) *Average	$E_{activation}$ (kJ/mol) Kissinger method	$E_{activation}$ (kJ/mol) Ozawa method
KNH20	917.8	81.1	1.4	52.4 (<150 °C) 42.8.0 (>150 °C)	55.9 (<150 °C) 47.6 (>150 °C)
NH20	1249.5	83.8	1.1	39.5	44.3
NS80	512.1	49.9	1.3	34.1	39.2
NS20	827.9	71.2	1.0	63.0	66.0

The results suggest that the dehydration enthalpy values calculated from the Kissinger method and the Ozawa method are similar, with the Ozawa method gives slightly higher

estimations. The TGA results show that, the dehydration peak temperature at heating rate 10K/min for NH20, NS20 and NS80 are 175 °C, 124 °C, and 187 °C, while the first and the second dehydration peak for KNH20 under the same conditions are 129 °C and 191 °C. The corresponded dehydration activation energy values are summarised in Table 4. The higher peak temperature correlates to the higher charging temperature while the higher activation energy corresponds to the higher energy barrier to initiate the dehydration process. For silica gel and hierarchically porous zeolites, the activation energy can be affected by both the surface textural and chemical properties, where smaller pore size and lower Si/Al ratio might lead to higher activation energy [55, 56]. However, for the four samples assessed, there seems to be no direct correlations between the textural properties and bulk Si/Al ratios. The structural order of the N(K)-A-S-H gel might be playing an important role in determining the activation energy which will need to be investigated in further studies. The NS20 has the lowest dehydration peak temperature but the highest activation energy. Comparing with the NS80, the partial crystallisation in N-A-S-H gel structure leads to increase of the charging temperature and decrease of activation energy. The two dehydration peaks observed from KNH20 sample is likely relating to the presence of two extra-framework cation Na^+ and K^+, where two different M(Na or K)-O-H water bonds might form [44, 57].

The molar dehydration enthalpy follows the order of NH20>KNH20>NS20>NS80, where the maximal value obtained from sample NH20 is similar to that reported for pure zeolite-X(Na) impregnate with 10wt.% of $MgCl_2$ [9]. Comparing with the performances of other porous thermochemical materials reported in literature, the amorphous N-A-S-H gel with bulk Si/Al ration of 1.5 (sample NS20) has higher molar dehydration enthalpy than zeolite-Y [9], clinoptilolite [58], silica gel and bentonite [7]. Sample NS20 and KNH20 have relatively similar mass energy density, with 827.9 $J/g_{dry\ mass}$ and 917.8 $J/g_{dry\ mass}$ respectively. These values are similar to acid-washed zeolite-Y impregnate with 5 wt.% to 15 wt.% $MgSO_4$ [59]. In comparison, it appears that partial crystallisation in geopolymers with higher Si/Al ratio (NS80) can significantly decrease the dehydration enthalpy.

4. Performances evaluation for heat storage

The energy performances of the four geopolymers assessed in this study are evaluated based on their theoretical volumetric heat storage capacities. The hydration heat storage capacities (HHSC) and the sorption heat storage capacities (SHSC) are calculated according to Eq. 5 and Eq. 6.

$$HHSC = \frac{\Delta H_{dehydration} \times \Delta M_{max}}{V} \quad \text{Eq. 5}$$

$$SHSC = \frac{\Delta H_{dehydration} \times \Delta M_{0\%-95\%}}{V} \quad \text{Eq. 6}$$

, where $\Delta H_{dehydration}$, ΔM_{max}, and V are the molar enthalpy of dehydration, the maximal molar amount of water uptake (from dehydration to equilibrium at 95% RH) for each 1 gram of the geopolymer (dry mass), and the volume of 1 gram of geopolymer paste (estimated as 0.625 cm^3/g for all samples [60]). The $\Delta M_{0\%-95\%}$ represent the molar amount of water uptake (from 0% RH to equilibrium at 95% RH) for each 1 gram of the geopolymer (dry mass), excluding the amount of water removable only via the heat drying process at 200 °C. The results are shown in Figure 9, together with the moisture diffusion coefficients at 50% relative humidity

calculated from the DVS results during desorption (as suggested as potentially preferable operation condition in section 3.3.).

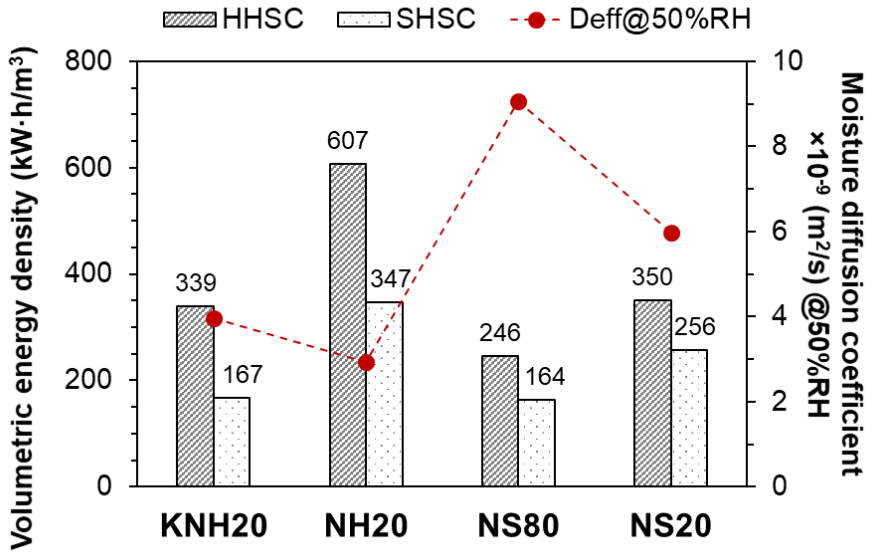

Figure 9 Volumetric energy density of hydration heat storage capacity (HHSC) and sorption heat storage capacity (SHSC) estimated for the four geopolymer samples, together with the moisture diffusion coefficient during desorption under targeted 50%RH.

The estimated volumetric energy density performances of these four geopolymer samples show that, for both HHSC and SHSC they follow that NH20>NS20>KNH20>NS80. Although NH20 has the highest volumetric energy density, its moisture diffusion coefficients during desorption at 50% RH, as well as the overall moisture diffusion coefficients, are the lowest among the four geopolymers assessed. This suggest that despite NH20 has the highest volumetric energy density, the low moisture diffusion coefficient might lead to slow charging/discharging kinetics resulting in low heating power. In comparison, NS20 has the second highest volumetric energy density as well as the second highest moisture diffusion coefficient, which might be able to provide the best overall energy storage performances, taking into consideration of both energy storage capacity and charging/discharging power. In comparison with other thermochemical energy storage materials, the theoretical energy storage performances of NS20 (350 kW h/m^3) is higher than some recently developed porous composite materials impregnated with salt hydrates [6, 61] with charging temperature suitable for concentrated solar collectors, as well as for medium temperature waste heat recovery [13, 61]. However, it is common that the operational energy storage performances under chosen operation conditions (e.g. relative humidity, pressure, gas flow rate etc.) can be lower than the maximal theoretical values [62]. Therefore, further test of the geopolymer materials at system level in the form of coarse particles and granules will need to be carried out, where the optimal operation conditions will need to be investigated as well.

5. Conclusion

This study proves that alkali-activated metakaolin geopolymers have the potential to be used as thermochemical heat storage materials for both sorption/desorption and hydration/dehydration thermal energy storage. The different chemical compositions, gel structures and textural properties of the geopolymers can all influence the energy storage performances, including the charging temperature, mass/volumetric energy storage capacity, as well as the charging kinetics (critical factor for heating power). The results of the four geopolymer samples assessed in this study suggest that:

- The bulk chemical compositions mainly determine the maximal amount of water uptake that can be achieved at 95% relative humidity under ambient pressure, where having lower Si/Al ratio and Na^+ being the sole activator cation resulted in higher water uptake capacities;
- The partial crystallisation of the amorphous N(K)-A-S-H gel, resulting in the formation of micropores, does not seem to affect the maximal water uptake but increases the proportion of the chemically bound water;
- Geopolymers with higher bulk Si/Al ratio exhibit higher moisture diffusion coefficients, suggesting faster charging/discharging capacity;
- The sodium hydroxide activated metakaolin geopolymer (NH20) achieved the highest maximal 1249.5 $J/g_{hydrate\ sample}$ (607 $kW{\cdot}h/m^3$) energy storage capacity at the charging temperature around 170 °C;
- The amorphous sodium aluminosilicate hydrate gel (N-A-S-H) can achieve the energy storage capacity of 827.9 $J/g_{hydrate\ sample}$ (350 $kW{\cdot}h/m^3$) with the lowest charging temperature (around 120 °C) among the four geopolymer samples assessed.

The outcomes of this study suggest that comparing with well crystallised zeolites, the main component of the geopolymers, the amorphous N(K)-A-S-H gels, have different water sorption/desorption, hydration/dehydration reaction kinetics and mechanisms, but with comparable energy storage performances. This implies that further tailoring and optimisation of the gel chemistry and structure will have the potential to achieve superior performances. The reversible water sorption/desorption performances of metakaolin geopolymers also suggest that such materials might also have the potential to be used as low-carbon desiccant materials. Future studies will be carried out in these directions.

Acknowledgement

The participate of XK is sponsored by the University of Bath Prize Fellowship. VAB acknowledges the Turkish Ministry of National Education for sponsoring his PhD study. The authors would also like to thank our senior laboratory technician Dr Olivier Camus for his help with collecting the DVS data, and Dr Gabriele Kociok-Köhn for her assistance with configurating the XRD testing program.

References

[1] T. Yang, A.K. Athienitis, A review of research and developments of building-integrated photovoltaic/thermal (BIPV/T) systems, Renewable and Sustainable Energy Reviews, 66 (2016) 886-912.

[2] Z. Ma, H. Bao, A.P. Roskilly, Seasonal solar thermal energy storage using thermochemical sorption in domestic dwellings in the UK, Energy, 166 (2019) 213-222.
[3] S. Hongois, F. Kuznik, P. Stevens, J.-J. Roux, Development and characterisation of a new MgSO4−zeolite composite for long-term thermal energy storage, Solar Energy Materials and Solar Cells, 95 (2011) 1831-1837.
[4] N. Hoivik, C. Greiner, J. Barragan, A.C. Iniesta, G. Skeie, P. Bergan, P. Blanco-Rodriguez, N. Calvet, Long-term performance results of concrete-based modular thermal energy storage system, Journal of Energy Storage, 24 (2019) 100735.
[5] Z. Tao, X. Chen, M. Yang, X. Xu, Y. Sun, Y. Li, J. Wang, G. Wang, Three-dimensional rGO@sponge framework/paraffin wax composite shape-stabilized phase change materials for solar-thermal energy conversion and storage, Solar Energy Materials and Solar Cells, 215 (2020) 110600.
[6] A.I. Shkatulov, J. Houben, H. Fischer, H.P. Huinink, Stabilization of K2CO3 in vermiculite for thermochemical energy storage, Renewable Energy, 150 (2020) 990-1000.
[7] A. Jabbari-Hichri, S. Bennici, A. Auroux, CaCl2-containing composites as thermochemical heat storage materials, Solar Energy Materials and Solar Cells, 172 (2017) 177-185.
[8] E. O'Dwyer, I. Pan, S. Acha, N. Shah, Smart energy systems for sustainable smart cities: Current developments, trends and future directions, Applied Energy, 237 (2019) 581-597.
[9] G.T. Whiting, D. Grondin, D. Stosic, S. Bennici, A. Auroux, Zeolite–MgCl2 composites as potential long-term heat storage materials: Influence of zeolite properties on heats of water sorption, Solar Energy Materials and Solar Cells, 128 (2014) 289-295.
[10] J. Cot-Gores, A. Castell, L.F. Cabeza, Thermochemical energy storage and conversion: A-state-of-the-art review of the experimental research under practical conditions, Renewable and Sustainable Energy Reviews, 16 (2012) 5207-5224.
[11] K. Johannes, F. Kuznik, J.-L. Hubert, F. Durier, C. Obrecht, Design and characterisation of a high powered energy dense zeolite thermal energy storage system for buildings, Applied Energy, 159 (2015) 80-86.
[12] J. Yan, Z.H. Pan, C.Y. Zhao, Experimental study of MgO/Mg(OH)2 thermochemical heat storage with direct heat transfer mode, Applied Energy, 275 (2020) 115356.
[13] P.A.J. Donkers, L.C. Sögütoglu, H.P. Huinink, H.R. Fischer, O.C.G. Adan, A review of salt hydrates for seasonal heat storage in domestic applications, Applied Energy, 199 (2017) 45-68.
[14] K. Ndiaye, M. Cyr, S. Ginestet, Durability and stability of an ettringite-based material for thermal energy storage at low temperature, Cement and Concrete Research, 99 (2017) 106-115.
[15] M. Gaeini, A.L. Rouws, J.W.O. Salari, H.A. Zondag, C.C.M. Rindt, Characterization of microencapsulated and impregnated porous host materials based on calcium chloride for thermochemical energy storage, Applied Energy, 212 (2018) 1165-1177.
[16] D. Mahon, G. Claudio, P.C. Eames, An experimental investigation to assess the potential of using MgSO4 impregnation and Mg2+ ion exchange to enhance the performance of 13X molecular sieves for interseasonal domestic thermochemical energy storage, Energy Conversion and Management, 150 (2017) 870-877.
[17] Q. Wang, Y. Xie, B. Ding, G. Yu, F. Ye, C. Xu, Structure and hydration state characterizations of MgSO4-zeolite 13x composite materials for long-term thermochemical heat storage, Solar Energy Materials and Solar Cells, 200 (2019) 110047.
[18] L. Tabard, E. Prud'Homme, V. Garnier, L. Gremillard, Hierarchical salt-ceramic composites for efficient thermochemical energy storage, Applied Materials Today, 20 (2020) 100658.

[19] A. Permyakova, S. Wang, E. Courbon, F. Nouar, N. Heymans, P. D'Ans, N. Barrier, P. Billemont, G. De Weireld, N. Steunou, M. Frère, C. Serre, Design of salt–metal organic framework composites for seasonal heat storage applications, Journal of Materials Chemistry A, 5 (2017) 12889-12898.
[20] K.E. N'Tsoukpoe, F. Kuznik, A reality check on long-term thermochemical heat storage for household applications, Renewable and Sustainable Energy Reviews, 139 (2021) 110683.
[21] J. Lizana, R. Chacartegui, A. Barrios-Padura, J.M. Valverde, Advances in thermal energy storage materials and their applications towards zero energy buildings: A critical review, Applied Energy, 203 (2017) 219-239.
[22] M. Röck, M.R.M. Saade, M. Balouktsi, F.N. Rasmussen, H. Birgisdottir, R. Frischknecht, G. Habert, T. Lützkendorf, A. Passer, Embodied GHG emissions of buildings – The hidden challenge for effective climate change mitigation, Applied Energy, 258 (2020) 114107.
[23] R. Horn, M. Burr, D. Fröhlich, S. Gschwander, M. Held, J.P. Lindner, G. Munz, B. Nienborg, P. Schossig, Life Cycle Assessment of Innovative Materials for Thermal Energy Storage in Buildings, Procedia CIRP, 69 (2018) 206-211.
[24] A.Z. Khalifa, Ö. Cizer, Y. Pontikes, A. Heath, P. Patureau, S.A. Bernal, A.T.M. Marsh, Advances in alkali-activation of clay minerals, Cement and Concrete Research, 132 (2020) 106050.
[25] N. Ye, J. Yang, X. Ke, J. Zhu, Y. Li, C. Xiang, H. Wang, L. Li, B. Xiao, Synthesis and Characterization of Geopolymer from Bayer Red Mud with Thermal Pretreatment, Journal of the American Ceramic Society, 97 (2014) 1652-1660.
[26] N. Kozhukhova, V. Strokova, I. Zhernovsky, K. Sobolev, Geopolymerization and Structure Formation in Alkali Activated Aluminosilicates with Different Crystallinity Degree, in: S. Glagolev (Ed.) 14th International Congress for Applied Mineralogy (ICAM2019), Springer International Publishing, Cham, 2019, pp. 331-334.
[27] J. Kiventerä, P. Perumal, J. Yliniemi, M. Illikainen, Mine tailings as a raw material in alkali activation: A review, International Journal of Minerals, Metallurgy and Materials, 27 (2020) 1009-1020.
[28] J.L. Provis, S.A. Bernal, Geopolymers and related alkali-activated materials, Annual Review of Materials Research, 44 (2014) 299-327.
[29] X. Ke, S.A. Bernal, J.L. Provis, Controlling the reaction kinetics of sodium carbonate-activated slag cements using calcined layered double hydroxides, Cement and Concrete Research, 81 (2016) 24-37.
[30] B. Pooja, G. Rainy, M. Deepti, M. Manish, A.S. Sitaram, Synthesis of advanced phosphatic geopolymers utilizing fly ash by way of greener route, Emerging Materials Research, 6 (2017) 168-177.
[31] J.L. Bell, P. Sarin, J.L. Provis, R.P. Haggerty, P.E. Driemeyer, P.J. Chupas, J.S.J. van Deventer, W.M. Kriven, Atomic Structure of a Cesium Aluminosilicate Geopolymer: A Pair Distribution Function Study, Chemistry of Materials, 20 (2008) 4768-4776.
[32] J.L. Provis, G.C. Lukey, J.S.J. van Deventer, Do geopolymers actually contain nanocrystalline zeolites? A reexamination of existing results, Chemistry of Materials, 17 (2005) 3075-3085.
[33] J.L. Bell, P. Sarin, P.E. Driemeyer, R.P. Haggerty, P.J. Chupas, W.M. Kriven, X-Ray pair distribution function analysis of a metakaolin-based, $KAlSi_2O_6{\cdot}5.5H2O$ inorganic polymer (geopolymer), J. Mater. Chem., 18 (2008) 5974-5981.
[34] C. Kuenzel, L.M. Grover, L. Vandeperre, A.R. Boccaccini, C.R. Cheeseman, Production of nepheline/quartz ceramics from geopolymer mortars, Journal of the European Ceramic Society, 33 (2013) 251-258.

[35] X. Guo, A. Navrotsky, Hydration dynamics in zeolite A – An X-ray diffraction and infrared spectroscopic study, Microporous Mesoporous Mater., 268 (2018) 197-201.
[36] F. Xiong, Z. Jiang, P. Li, X. Wang, H. Bi, Y. Li, Z. Wang, M.A. Amooie, M.R. Soltanian, J. Moortgat, Pore structure of transitional shales in the Ordos Basin, NW China: Effects of composition on gas storage capacity, Fuel, 206 (2017) 504-515.
[37] P.C. Hansen, D.P. O'Leary, The Use of the L-Curve in the Regularization of Discrete Ill-Posed Problems, SIAM Journal on Scientific Computing, 14 (1993) 1487-1503.
[38] X. Yu, A.R. Schmidt, L.A. Bello-Perez, S.J. Schmidt, Determination of the Bulk Moisture Diffusion Coefficient for Corn Starch Using an Automated Water Sorption Instrument, Journal of Agricultural and Food Chemistry, 56 (2008) 50-58.
[39] H.V. Thang, L. Grajciar, P. Nachtigall, O. Bludský, C.O. Areán, E. Frýdová, R. Bulánek, Adsorption of CO2 in FAU zeolites: Effect of zeolite composition, Catalysis Today, 227 (2014) 50-56.
[40] K. Muraoka, Y. Sada, A. Shimojima, W. Chaikittisilp, T. Okubo, Tracking the rearrangement of atomic configurations during the conversion of FAU zeolite to CHA zeolite, Chemical Science, 10 (2019) 8533-8540.
[41] M. Król, J. Minkiewicz, W. Mozgawa, IR spectroscopy studies of zeolites in geopolymeric materials derived from kaolinite, Journal of Molecular Structure, 1126 (2016) 200-206.
[42] B. Walkley, X. Ke, O.H. Hussein, S.A. Bernal, J.L. Provis, Incorporation of strontium and calcium in geopolymer gels, Journal of Hazardous Materials, (2019) 121015.
[43] X. Ke, J.L. Provis, S.A. Bernal, Structural ordering of aged and hydrothermally cured metakaolin based potassium geopolymers, Springer Netherlands, Dordrecht, 2018, pp. 232-237.
[44] M. Król, W. Mozgawa, W. Jastrzębski, K. Barczyk, Application of IR spectra in the studies of zeolites from D4R and D6R structural groups, Microporous Mesoporous Mater., 156 (2012) 181-188.
[45] X. Ke, S.A. Bernal, N. Ye, J.L. Provis, J. Yang, One-Part Geopolymers Based on Thermally Treated Red Mud/NaOH Blends, Journal of the American Ceramic Society, 98 (2015) 5-11.
[46] V. Benavent, F. Frizon, A. Poulesquen, Effect of composition and aging on the porous structure of metakaolin-based geopolymers, Journal of Applied Crystallography, 49 (2016) 2116-2128.
[47] K. Yang, C.E. White, Multiscale pore structure determination of cement paste via simulation and experiment: The case of alkali-activated metakaolin, Cement and Concrete Research, 137 (2020) 106212.
[48] J.M. Haynes, Pore size analysis according to the Kelvin equation, Matériaux et Construction, 6 (1973) 209-213.
[49] H. Kim, H.J. Cho, S. Narayanan, S. Yang, H. Furukawa, S. Schiffres, X. Li, Y.-B. Zhang, J. Jiang, O.M. Yaghi, E.N. Wang, Characterization of Adsorption Enthalpy of Novel Water-Stable Zeolites and Metal-Organic Frameworks, Scientific Reports, 6 (2016) 19097.
[50] A. Zolfaghari, H. Dehghanpour, M. Xu, Water sorption behaviour of gas shales: II. Pore size distribution, International Journal of Coal Geology, 179 (2017) 187-195.
[51] J.C. Groen, L.A.A. Peffer, J. Pérez-Ramírez, Pore size determination in modified micro- and mesoporous materials. Pitfalls and limitations in gas adsorption data analysis, Microporous Mesoporous Mater., 60 (2003) 1-17.
[52] C.I. Fialips, J.W. Carey, D.L. Bish, Hydration-dehydration behavior and thermodynamics of chabazite, Geochimica et Cosmochimica Acta, 69 (2005) 2293-2308.
[53] H.E. Kissinger, Variation of Peak Temperature With Heating Rate in Differential Thermal Analysis, Journal of Research of the National Bureau of Standards, 57 (1956) 2712.

[54] T. Ozawa, Kinetic analysis of derivative curves in thermal analysis, Journal of thermal analysis, 2 (1970) 301-324.
[55] X. Wei, W. Wang, J. Xiao, L. Zhang, H. Chen, J. Ding, Hierarchically porous aluminosilicates as the water vapor adsorbents for dehumidification, Chemical Engineering Journal, 228 (2013) 1133-1139.
[56] X. Li, Z. Li, Q. Xia, H. Xi, Effects of pore sizes of porous silica gels on desorption activation energy of water vapour, Applied Thermal Engineering, 27 (2007) 869-876.
[57] M. Zema, S.C. Tarantino, G. Montagna, Hydration/Dehydration and Cation Migration Processes at High Temperature in Zeolite Chabazite, Chemistry of Materials, 20 (2008) 5876-5887.
[58] N. Petrova, T. Mizota, K. Fujiwara, Hydration Heats of Zeolites For Evaluation of Heat Exchangers, Journal of Thermal Analysis and Calorimetry, 64 (2001) 157-166.
[59] G. Whiting, D. Grondin, S. Bennici, A. Auroux, Heats of water sorption studies on zeolite–MgSO4 composites as potential thermochemical heat storage materials, Solar Energy Materials and Solar Cells, 112 (2013) 112-119.
[60] N.A. Jaya, L. Yun-Ming, H. Cheng-Yong, M.M.A.B. Abdullah, K. Hussin, Correlation between pore structure, compressive strength and thermal conductivity of porous metakaolin geopolymer, Construction and Building Materials, 247 (2020) 118641.
[61] L. Lavagna, D. Burlon, R. Nisticò, V. Brancato, A. Frazzica, M. Pavese, E. Chiavazzo, Cementitious composite materials for thermal energy storage applications: a preliminary characterization and theoretical analysis, Scientific Reports, 10 (2020) 12833.
[62] S.P. Casey, J. Elvins, S. Riffat, A. Robinson, Salt impregnated desiccant matrices for 'open' thermochemical energy storage—Selection, synthesis and characterisation of candidate materials, Energy and Buildings, 84 (2014) 412-425.